220-to-330-GHz Manifold Triplexer With Wide Stopband Utilizing Ridged Substrate Integrated Waveguides

Jack W. Holloway, *Member, IEEE*, Georgios C. Dogiamis, *Member, IEEE*, Sanghoon Shin, *Senior Member, IEEE*, and Ruonan Han, *Senior Member, IEEE*

***Abstract*— This article reports a three-channel, noncontiguous, manifold multiplexer operating from 220 to 330 GHz, a 40% fractional operating bandwidth. The structure is designed and implemented using a set of ridged substrate integrated waveguides (SIWs). The ridged SIW improves the stopband bandwidth and reduces the overall structure size by 35% over a conventional SIW design. The triplexer utilizes an organic package substrate technology developed by Intel, featuring four thick copper metal layers and continuous trench vias in lieu of standard via fences, which significantly decrease the ohmic loss of the ridged SIW waveguides. Electromagnetic-circuit modeling and codesign techniques are adopted in the development of the triplexer structure. The fabricated triplexer is measured using banded millimeter-wave wafer probing and exhibits 3∼7 dB of insertion loss in the passbands and better than 10 dB of average return loss for each of the channel filters. The measured stopband attenuation is better than 27 dB for all three channels.**

***Index Terms*— Channelizer, manifold multiplexer, multiplexer, ridge substrate integrated waveguide (SIW), terahertz, triplexer.**

I. Introduction

With the growing interest in millimeter-wave and terahertz (THz) electronics, there has been an associated interest in the various components that are required to realize these systems. In [1], one application of these systems is described, in which guided and modulated sub-THz (approximately 220–330 GHz) waves are used to transport high-rate data over backplane-scale distances. Such a scheme is attractive for a number of reasons, including broad available fractional bandwidth, compact system size (driven by smaller wavelengths compared with lower frequency operations), relative robustness to misalignment during assembly versus optical systems, and lower transmission losses than those exhibited by copper lines for high-speed data transmission.

One of the challenges associated with the development of the above link system is the realization of compact, low-loss channelizers. The use of these components is a fundamental requirement to leverage the available waveguide bandwidths. While waveguide-based channelizers have been demonstrated at lower bands and waveguide components are available at higher operating frequencies, they are relatively large and require more expensive packaging and interface schemes. This type of scheme would require a planar integration approach to be economically feasible. On-chip implementation is one option: the use of transmission line-based structures in an integrated circuit (IC) back end of line (BEOL) can produce compact filters, but the loss associated with radiation and conductor resistance is a disadvantage. Substrate integrated waveguide (SIW) filters have been broadly investigated at lower frequencies [2]–[5] for their superior performance over other planar approaches. There are some published results of BEOL-integrated SIW structures for radiators in the sub-THz regime [6]–[11] and a smaller number related to transmission lines [12] and simple filters [13]. There are a few published SIW filter works utilizing LTCC or PCB materials at W-band [14], [15] and above [16]. In [17], a novel thick-film technology was used to demonstrate cavity filters at V-, W-, D-, and G-bands. In comparison to single filter topologies, the use of SIW topologies and techniques for RF multiplexers and channelizers has been relegated to lower frequencies [18], [19]. This may be attributed to the difficulty of designing both manifold [20] and star-junction [21] devices, as well as the design rules and tolerances in available processes.

This article discusses the design and measurement of a 220–330-GHz triplexer for the integration into a high data rate meter-class I/O scheme illustrated in Fig. 1. The concept is shown in further detail in the figure inset in which a flip-chip bonded IC with sub-THz transceivers is directly connected to an in-package multiplexer to combine (on transmit) and channelize (on receive) the modulated sub-THz wave. The multichannel sub-THz energy is coupled to/from the sub-THz

Manuscript received February 4, 2020; revised April 21, 2020; accepted May 8, 2020. Date of publication June 15, 2020; date of current version August 5, 2020. This work was supported in part by Intel Corporation through a Semiconductor Research Corporation (SRC) Member Specific Research Grant to the Massachusetts Institute of Technology (MIT) under Grant 2017-IN-2752 and in part by the Raytheon Advanced Study Program. *(Corresponding author: Jack W. Holloway.)*

Jack W. Holloway is with the Department of Electrical Engineering and Computer Science, Massachusetts Institute of Technology (MIT), Cambridge, MA 20139 USA, and also with Raytheon Technologies, Raytheon Missiles & Defense, Tewksbury, MA 01876 USA (e-mail: holloway@mit.edu).

Georgios C. Dogiamis is with the Components Research Team, Intel Corporation, Chandler, AZ 85226 USA (e-mail: georgios.c.dogiamis@intel.com).

Sanghoon Shin is with the Naval Research Laboratory, Washington, DC 20375 USA (e-mail: sanghoon.shin@nrl.navy.mil).

Ruonan Han is with the Department of Electrical Engineering and Computer Science, Massachusetts Institute of Technology (MIT), Cambridge, MA 20139 USA (e-mail: ruonan@mit.edu).

Color versions of one or more of the figures in this article are available online at http://ieeexplore.ieee.org.

Digital Object Identifier 10.1109/TMTT.2020.2997367

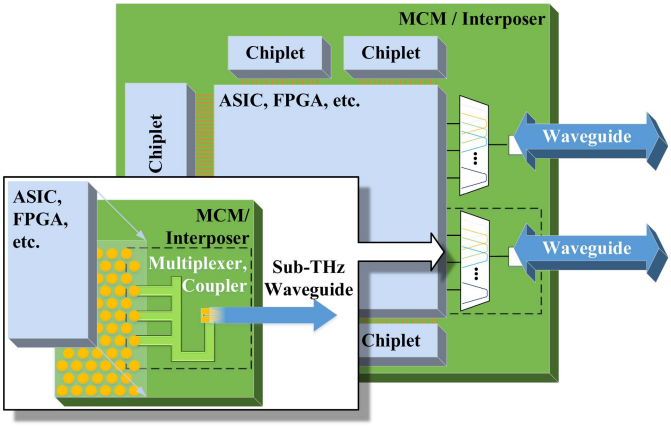

Fig. 1. Concept of a multichip module (MCM) in which high-rate data are aggregated and transported across a wideband sub-THz dielectric waveguide. Inset: exploded view of the concept with a broadband triplexer, directly coupled to solder bumps, each driven by an electronic sub-THz transceiver. The combined energy is coupled into a sub-THz waveguide via a broadband coupler. The triplexer structure is outlined in the dotted black line within the inset.

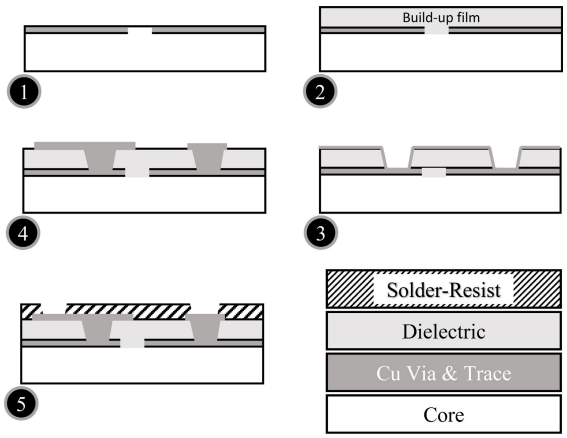

(a)

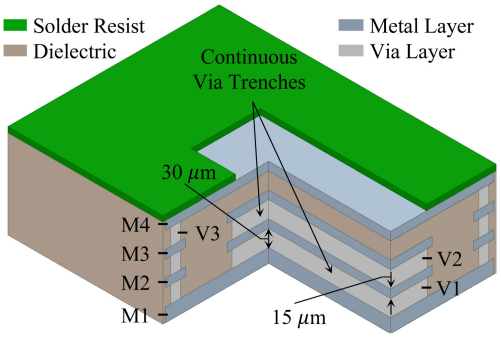

(b)

Fig. 2. (a) Simplified semiadditive microelectronics packaging process flow for N buildup dielectric layers. (b) Graphic illustration of the cross section of the organic packaging process with an integrated ridge (implemented using layers M1–M3 and V1 and V2).

waveguide via a wideband planar coupler [6]. To the best of our knowledge, there was previously no work utilizing SIW structures for channelizing sub-THz signals.

This triplexer is implemented in a new organic packaging process technology developed by Intel Corporation. This new process features thick copper layers, continuous via bars/trenches, and flexible design rules. The channelizer, based on a manifold topology [20], [22], uses ridged SIW structures for the individual channel filters and includes broadband ground–signal–ground (GSG) transitions for direct wafer probing. The device is designed for three 30-GHz-wide passbands with 10-GHz guard bands between channels.

II. Organic Packaging Process

The triplexer presented in this work is fabricated on an IC organic packaging process developed at Intel Corporation employing laminate panels of $\sim 500 \times 500$ mm^2 area. The fabrication process is a modified semiadditive microelectronics packaging process (SAP) that allows the creation of continuous and arbitrary shape interlayer trench vias. A high-level fabrication flow of a semiadditive microelectronics packaging process is shown in Fig. 2(a). The process starts with a patterned copper clad core (CCL) with through holes (step 1). Next, the dielectric buildup film is laminated (step 2). Laser via drilling, cleaning, and seed deposition follows (step 3). Via and trace formation are performed via plating and etching (step 4). Steps 2–4 are repeated for N metal layers. Finally, solder-resist layer deposition and patterning are performed (step 5).

The developed stack-up features a total of eight metal layers and three buildup dielectric layers around each side of a thicker substrate core. The buildup layers feature low-loss organic-based materials with inorganic fillers, while the top and bottom sides of the fabricated package are covered by a solder-resist layer. The dielectric layer and the core layer thicknesses targeted are 30 and 200 μm, respectively. The targeted copper thickness is 15 μm. Continuous trench vias, favored for the implementation of low-loss SIW structures, are enabled through lithographic processes. These via layers target 30 μm in thickness. Fig. 2(b) shows a cross section of the metal layers (M1–M4) and interlayer vias (V1–V3) utilized in this article. A ridge structure is also shown in the figure.

III. Triplexer Design

The triplexer is designed to match to 50 Ω at all ports and has three 30-GHz-wide channels: 220–250 GHz (Channel 1), 260–290 GHz (Channel 2), and 300–330 GHz (Channel 3). For the application described in Fig. 1, less than 5 dB of passband insertion loss and better than 10 dB return loss are desired. To prevent cross-channel interference, more than 30 dB of stopband attenuation and better than 40 dB of interchannel isolation are also required.

Fig. 3 shows a 3-D model of the final triplexer design. The structure makes use of ridged SIW resonator sections, as described in Section III-A. The individual channel filters and the manifold (common) ports are excited with wideband transitions from GSG probes [see Fig. 3 (upper right inset)]. This transition is described in Section III-B. Finally, a very fast circuit-EM codesign scheme is described in Section III-C to finalize the triplexer dimensional parameters.

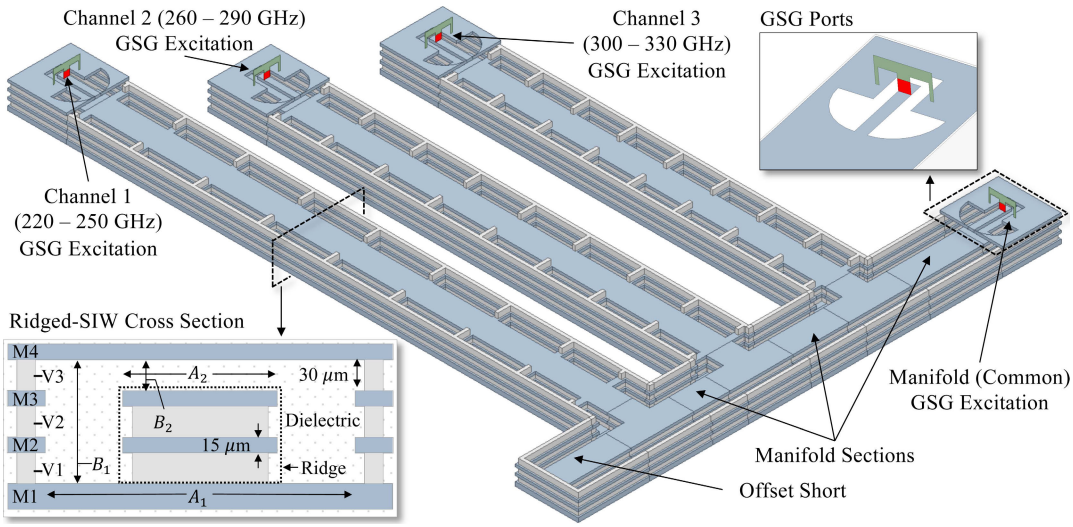

Fig. 3. Isometric view of a model of the final 220–330-GHz triplexer design. The process' top metal layer, M4, and the dielectric fill material have been removed from the model to reveal the structural details of the channel filters, T-junctions, and connecting manifold. The three-channel filter GSG ports are illustrated, along with the manifold GSG port. The lower left inset shows a cross section of the ridged-SIW resonator sections. The upper right inset shows a detail on the GSG ports used to simulate and measure the device.

A. SIW Versus Ridged-SIW

Due to the large range of frequencies over which the triplexer must operate, consideration must be given to the spurious passband present in a bandpass filter utilizing a conventional SIW with a rectangular cross section [23], [24]. This leads to an unwanted interaction between Channels 1 and 3. In order to ameliorate this problem, a ridged-waveguide topology is adopted, which takes advantage of the wider frequency range over which only the lowest order mode is allowed to propagate [25], [26]. A ridged waveguide has a wider spurious-free passband region over the conventional rectangular waveguide (RWG). Since the cross-sectional circumference of a ridged waveguide is much longer than an RWG due to the additional ridge inside the waveguide, the associated cutoff frequency is much lower than that of the RWG with the same size. Due to an irregular shape of the inside of the ridged waveguide [see Fig. 2(b)], the transverse resonance method can be used to analyze the structure. The cutoff frequency of a single ridged waveguide can be found by using [27]

$$f_c = \frac{1}{2A_1\sqrt{\mu\epsilon}} \cdot \frac{2}{\pi}\sqrt{\frac{A_1}{A_2}\frac{B_2}{B_1}\frac{1}{1-\frac{A_2}{A_1}}} \tag{1}$$

where μ and ϵ are the permeability and permittivity of the process dielectric material, and A_1, A_2, B_1, and B_2 are the guide dimensions shown in the inset of Fig. 3. In addition, the gap between the top surface of the ridge and the waveguide ground surface has a strong electric field; this capacitive loading increases the cutoff frequency of the next higher mode operation compared with the case of an RWG-based resonator. Such a cutoff frequency can be modified by the values of these dimensional parameters B_2 and A_2. By leveraging this wider fundamental-mode bandwidth provided by ridged-waveguide resonators, we realize higher spurious-free stopband suppression than with conventional RWGs (or SIWs). However, the structure does incur additional insertion loss over conventional RWG-based filters.

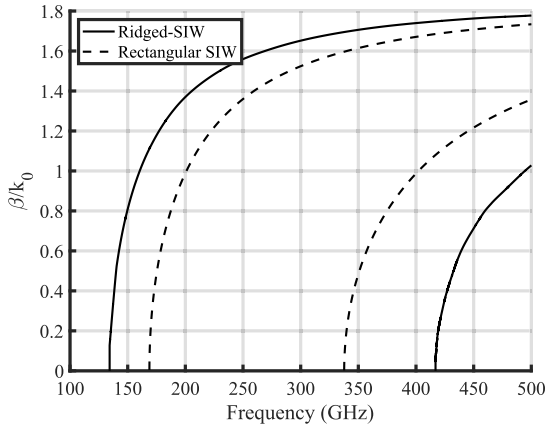

Fig. 4. Eigenmode simulation of a ridged-SIW section versus a standard rectangular SIW section.

As the packaging process provides access to variable ridge heights by using different metal layers, a parametric eigenmode analysis using HFSS [28] is carried out to determine the optimal dimensions for the maximum quality factor Q of an idealized resonator geometry. An overall guide width of A_1=300 μm [see Fig. 3 (inset)] and height of B_1=120 μm (utilizing the full process stack) are adopted. A ridge width of 50% of the overall waveguide width (to meet spurious passband requirements) and a ridge height of 90 μm (commensurate with the M3 metal layer) are found to provide the highest available Q: between 233 and 238 across the entire triplexer operating band, including dielectric and conductor losses. These dimensions were used on the subsequent channel filter and triplexer designs. Fig. 4 shows the waveguide dispersion results of an eigenmode simulation in which the normalized propagation constants β/k_0 of the first two modes are plotted.

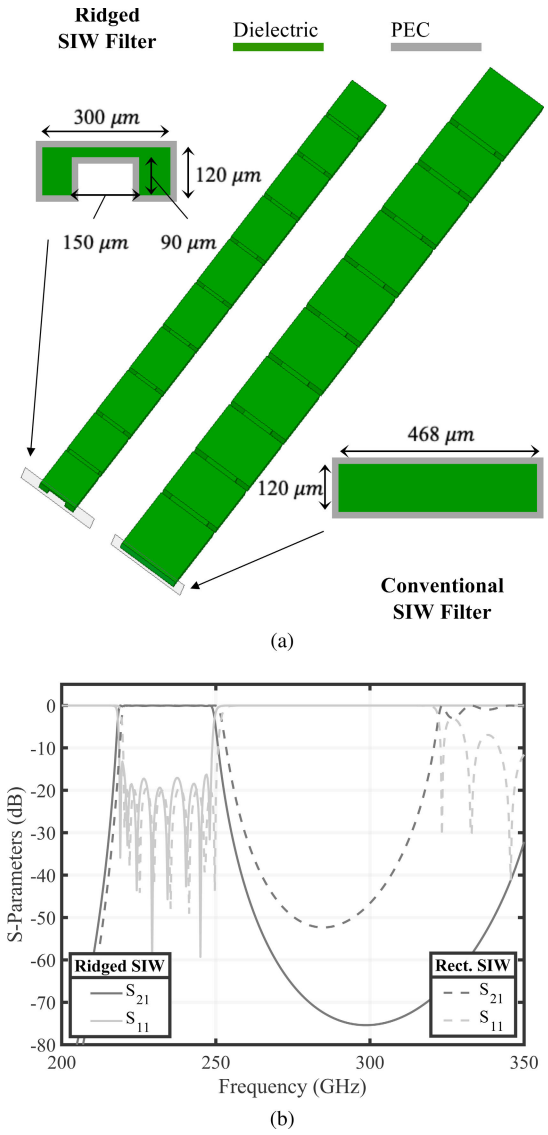

Fig. 5. Full-wave EM simulation of idealized conventional SIW and ridged-SIW filter. (a) Isometric views of the two topologies along with the cross sections of the respective resonant sections; the PEC surrounding the filter structures is removed in the isometric views, revealing the internal dielectric material. (b) S-parameters demonstrating suppression of the unwanted spurious passband.

As can be seen, only the lowest-order mode is supported from 130 to 410 GHz using this ridged SIW cross section, providing 280 GHz of available single-mode bandwidth—far more than the 110 GHz required in this channelizer design. Rectangular SIW dispersion characteristics are also shown for comparison. In this case, the ridged cross section provides a 67% more single-mode bandwidth than the rectangular SIW.

For comparison, a conventional RWG-based SIW filter and a ridged-SIW-based filter, both having eight sections and eight passband poles, are designed using FEST3D [29]. Both filter designs maintain compatibility with the dimensions available in the organic packaging process described in Section II, and they are optimized to meet the same passband bandwidth, insertion loss, match, and adjacent band suppression figures. As shown in Fig. 5(a), the ridged SIW filter is ∼40% more compact. The resultant 3-D structures are simulated using HFSS. The simulated S-parameters are shown in Fig. 5(b) and verify that the ridged-SIW topology indeed improves the spurious passband performance by >50 dB and increases the adjacent channel stopband suppression by ∼10–25 dB across the 260-to-290 GHz band.

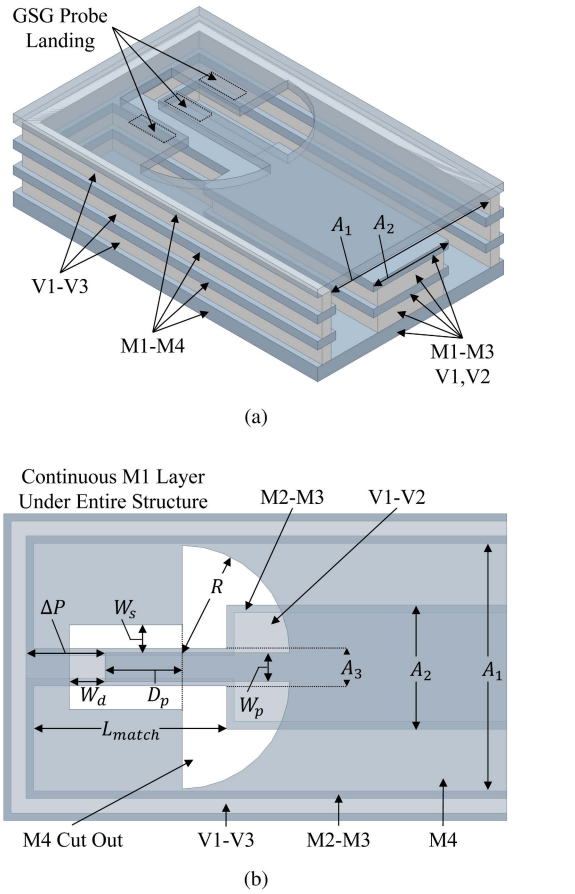

Fig. 6. (a) Isometric view and (b) top view of the broadband GSG to ridged-SIW transition. The dielectric filled in the structure is not shown.

B. Wideband Ridged-SIW to GSG Transition

In order to measure the triplexer in the WR-3.4 band, transitions to GSG pads for on-substrate probing had to be integrated. To facilitate rapid design, a single wideband transition was designed into the packaging process, simultaneously providing the pads for probing, waveguide mode conversion, and impedance matching. An approach based on the technique presented in [30] was used. In the previous work, a short section of slot line was used to produce the match between a GSG probe and an SIW at W-band. As the presented triplexer operates over a large fractional bandwidth (40%), a broader bandwidth match was required.

Fig. 6(a) shows the transition structure. The top metal layer was used to realize the pad landings. The pads are terminated with broadband opens realized as circular slots. The interposer process provides flexible conductor design rules, including curved geometries. This flexibility allows for the design of this type of broadband open termination. A symmetric lumped port

TABLE I
DIMENSIONS OF THE GSG PADS TO RIDGED-SIW TRANSITION

Parameter	Dimension (μm)	Parameter	Dimension (μm)
A_1	300	A_2	150
A_3	45.7	R	130
D_p	93.5	L_{match}	330
W_d	43.1	W_p	35
W_s	33.8	ΔP	113

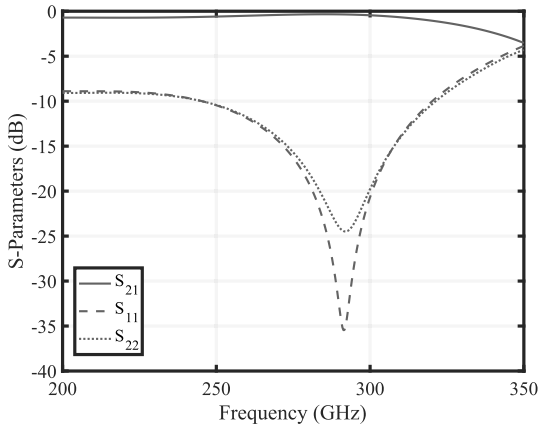

Fig. 7. Full-wave simulated S-parameters of the wideband GSG-to-ridged-SIW transition, designed in the interposer process. Port 1 corresponds to the GSG probe port, and port 2 corresponds to the ridged SIW port.

mimicking the wafer probe is used to excite the GSG pads. The values of the dimensional parameters [as illustrated in Fig. 6(b)] of the transition are listed in Table I.

Fig. 7 shows the simulated S-parameters of the transition. Across the entire 200-to-320-GHz band, the return loss is better than 8 dB, and the insertion loss is better than 3 dB. The slight mismatch below 250 GHz and above 320 GHz was compensated in the final design by absorbing the transition response into the final triplexer end-to-end response.

C. EM-Circuit Model Codesign

Full-wave parametric design and optimization of complicated electromagnetic structures can be time consuming and expensive. Assuming a triplexer utilizing asymmetric eight-pole channel filters, the overall triplexer would require tuning over at least 61 parameters. This figure includes nine iris widths and ten waveguide lengths per channel filter and four manifold spacing lengths between each of the channel filters.

Instead, a method, which is based on an EM-circuit codesign and similar to that presented in [18] and [31], was utilized to rapidly converge on a set of design parameters. In this case, a waveguide cross section was first set ($A_1 = 300$ μm and $A_3 = 150$ μm in Table I), and a straight section of ridged SIW was modeled with an inductive iris. This iris width was varied, and broadband full-wave simulations were performed in HFSS, with waveport deembedding used to move the reference plane immediately adjacent to the iris (see Fig. 8). In addition, a ridged SIW T-junction was modeled and deembedded ($\mathbf{S_T}$) to remove the response of a feed waveguide with a finite length.

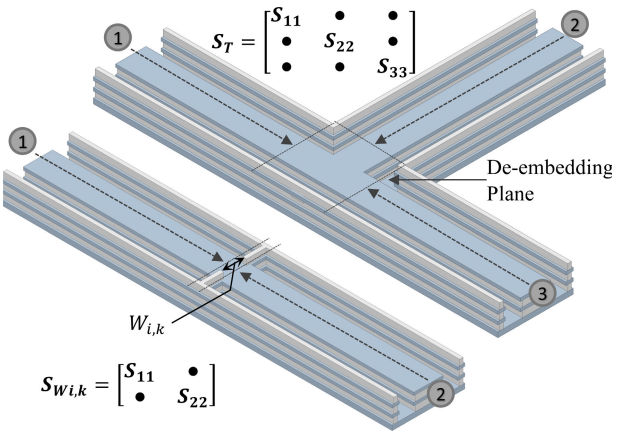

Fig. 8. Full-wave models of ridged-SIW building blocks. Parametrically varied inductive iris widths are used to model $\mathbf{S_{Wi,k}}$, and a ridged-SIW T-junction to model $\mathbf{S_T}$. The top copper layer is removed from the isometric images to reveal features within the structures. The arrows in the overhead views denote the full-wave deembedding to the ultimate block reference planes.

The resultant parameterized S-parameter files are used in a circuit simulator to model the reactive response of the iris, $\mathbf{S_{Wi,k}}$ corresponding to the frequency response of the kth iris in the ith filter with iris opening width $W_{i,k}$ (see Fig. 9). The responses of lengths of ridged-SIW (corresponding to parameter $L_{i,k}$ in Figs. 9 and 10) are based on a port-only full-wave solution for the guide cross section, with the propagation constant and attenuation (β and α, respectively) extracted. These transmission line responses are modeled in the same circuit simulator, parameterized by guide length. These parameterized iris responses were integrated into a full triplexer circuit model (see Fig. 10) incorporating the wideband GSG probe transition $\mathbf{S_P}$ and the T-junction response $\mathbf{S_T}$.

Each channel filter is connected through a certain length of single-ridge waveguide ($L_{i,1}$ in Fig. 10) to provide a proper phase compensation between channel filters. The connecting manifold lengths (L_{32}, L_{21}, and L_{short}) are determined to provide an open-matching in the center frequency of the neighboring channels.

Interpolation of the previously generated iris responses, $\mathbf{S_{Wi,k}}$, was utilized in the S-parameter circuit simulation to rapidly optimize the triplexer parameters in the circuit domain. The triplexer was optimized for a flat passband and return loss. A 10-GHz guard band was utilized between each channel, and the design was optimized for better than 10-dB return loss at the output of each channel filter. The resultant circuit simulator-generated dimensions were utilized in a fully parameterized full-wave model of the overall design (as shown in Fig. 3). The results for both the circuit-EM model and the full-wave model are plotted in Fig. 11. It should be noted that no postcircuit-design optimization was done utilizing the full-wave model. As the full-wave simulation of the entire triplexer structure required orders of magnitude more time (more than an hour compared with fractions of a minute when utilizing the circuit model), further full-wave optimization was not practical. The results show excellent agreement between the two simulated responses.

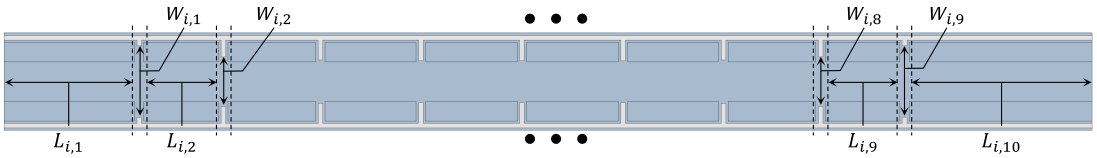

Fig. 9. Top view of a full-wave model of a parameterized, asymmetric, eight-pole ridged-SIW bandpass filter utilizing inductive iris coupling. The structure's top copper layer is removed in this view to reveal structure within the filter.

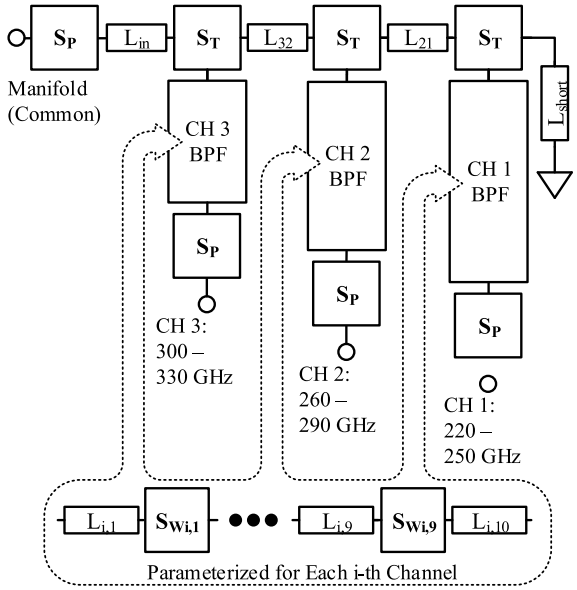

Fig. 10. Circuit model used in the EM-circuit codesign of the presented triplexer. Each bandpass filter is composed of fully parameterized lengths of waveguide and S-parameters, parameterized by width, representing the inductive irises.

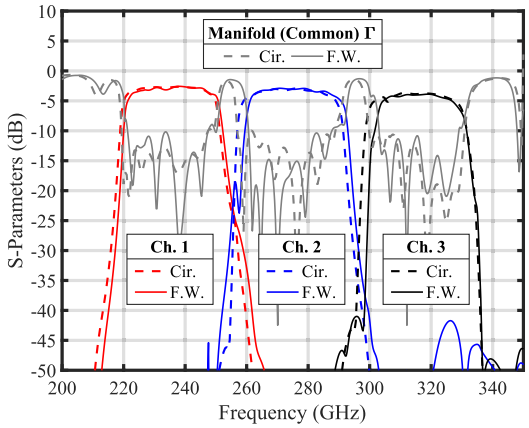

Fig. 11. Comparison of the simulated responses of the circuit-EM codesign triplexer (dashed lines) and the full-wave triplexer response (solid lines).

The manifold reflection Γ, as shown in Fig. 11, shows a good match across all the designed passbands, with a reflection between the passbands. This is expected given the noncontiguous design. In addition, the full-wave model was used to generate plots of the magnitude of the E-field on all the device conductors in Fig. 12. The three plots demonstrate the passband characteristics of the device at the designed center frequencies of the three channels. Fig. 12 also demonstrates that the channel filters effectively suppress the out-of-band energy injected into the channelizer from the manifold or the other channel filters.

IV. Experimental Results

A. Fabrication

All designs were fabricated at a facility in Intel Corporation, Chandler, AZ, USA. The process provides a feasible means to realize highly scalable, higher performance electromagnetic structures. Fig. 13(a) shows a fabricated panel, sized 500 mm × 500 mm, made up of copies of designed test structures. A 3-D X-ray view of the fabricated triplexer is shown in Fig. 13(b). A photograph of a portion of the fabricated devices, with the triplexer and individual channel filter locations denoted, is shown in Fig. 14. The GSG pads and the wideband ridged-SIW transitions implemented in the top copper layer are revealed through the solder-resist layer openings.

B. Individual Channel Measurements

Three individual channel filters [see Fig. 14 (left)] incorporating wideband GSG transitions on both sides of the filter structure were fabricated and measured. These filter designs are identical to the channel filters optimized for use in the triplexer. When measuring the individual channel filters, the probes are colinear. This colinear geometry also allows the use of standard one-tier probe calibration using commercially available calibration standards.

The measured and simulated data are plotted in Fig. 15. There is good agreement between the number and location of the passband poles, indicated by the location of the resonances in the input reflections (S_{11}, S_{22})—especially in the lower two channels. The measured data are within 2–4 dB of the simulated passband S_{21} in the bottom two channels. The top channel [see Fig. 15(c)] demonstrates a larger discrepancy between the simulated and measured data of up to 7 dB in the mid-band.

Unanticipated out-of-band resonances can be seen in all three measurements (S_{11}, S_{22}, and S_{21}) outside of the individual channel passbands. For example, in Fig. 15(a), we see a discrepancy due to a passband pole at approximately 260 GHz. Similarly, in Fig. 15(b), unintended passband poles are placed outside the desired passband (260–290 GHz) at approximately 240 and 305 GHz. We also see an unintended transmission in channel 3 [see Fig. 15(c)] at approximately 255 GHz. Given the exact number of resonators in each filter, we assess that these unanticipated portions of the responses

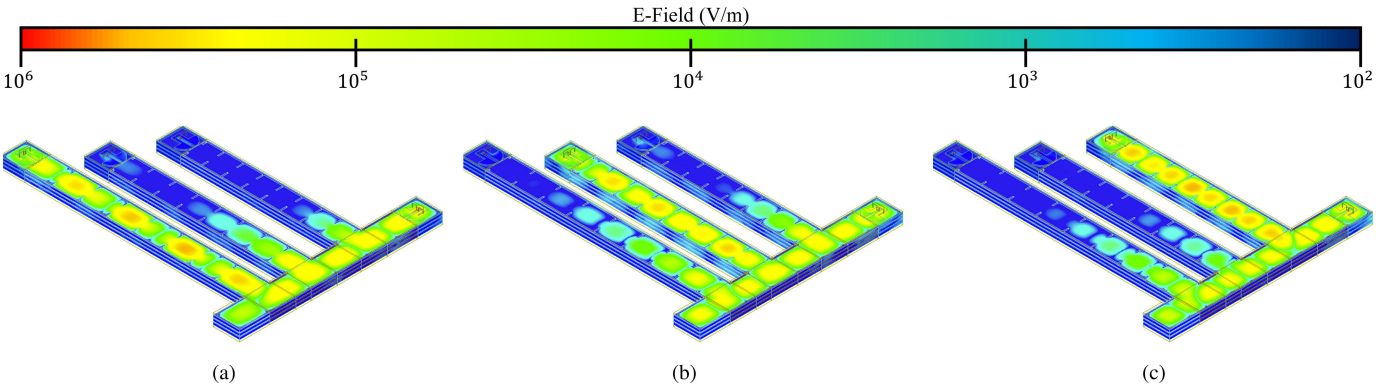

Fig. 12. Plot of the E-field intensity on the triplexer conductor surfaces at (a) 235, (b) 275, and (c) 315 GHz. These frequencies correspond to the centers of the three passband channels.

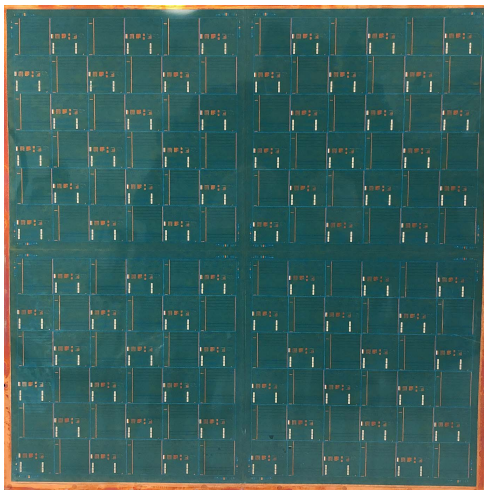

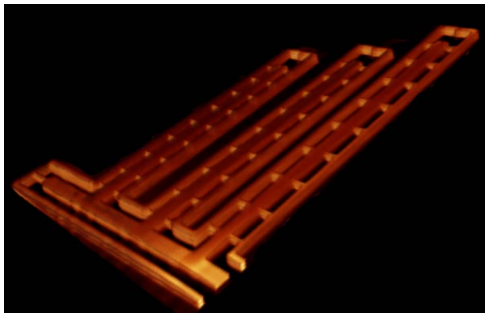

Fig. 13. (a) Fabricated 500 mm × 500 mm panel made up of repeated test designs. (b) 3-D X-ray image of the fabricated triplexer on Intel's organic packaging process. Note that the top and bottom metal layers have been intentionally hidden to allow a view of the internal ridges and SIW resonator cavities.

are due to slightly misplaced passband poles. These effects are due to either small differences in the packaging dielectric properties, small perturbations in the fabricated devices (vertically or laterally), or both. These unanticipated responses are responsible for the reduction in the measured passband bandwidths and the poorer input match compared with the simulated response.

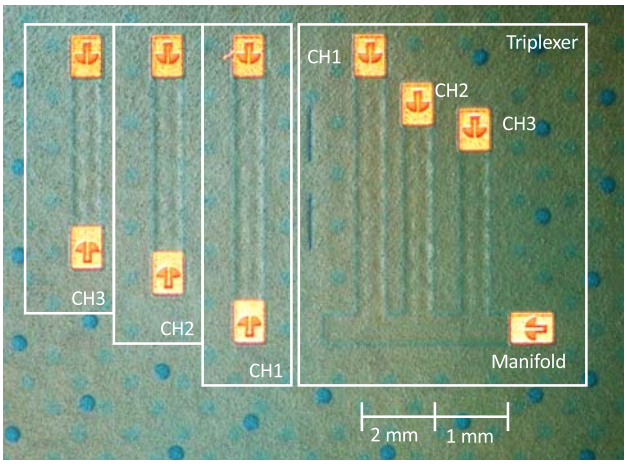

Fig. 14. Micrograph of the standalone channel filters (left) and the complete triplexer (right).

C. Triplexer Measurement

The frequency of operation precludes performing measurements with more than two ports. In addition, the design did not include resistors, and the use of discrete resistors at these frequencies is impractical. These factors dictated two-port measurements with the remaining device ports unterminated (open).

As can be seen in the photograph in Fig. 14, the manifold and individual channel filters in the triplexer are not colinear. The device testing is done via 100-μm-pitch wafer probes; at these frequencies, no commercially available calibration substrates are available that account for the 90° relative orientation between the channel filters and the triplexer manifold. Instead, a tiered calibration scheme was utilized to calibrate the probe tips. As described in Section III, the response of the wideband GSG probe to ridged-SIW transition was absorbed into the overall triplexer response. This allows the full device response to be tested by simply calibrating the wafer probe tips.

The test setup, pictured in Fig. 16, consists of a Keysight PNA-X four-port Vector Network Analyzer (VNA), two Virginia Diodes (VDIs) WR-3.4 frequency extenders, and two Cascade Infinity WR-3.4 GSG probes. Several straight sections

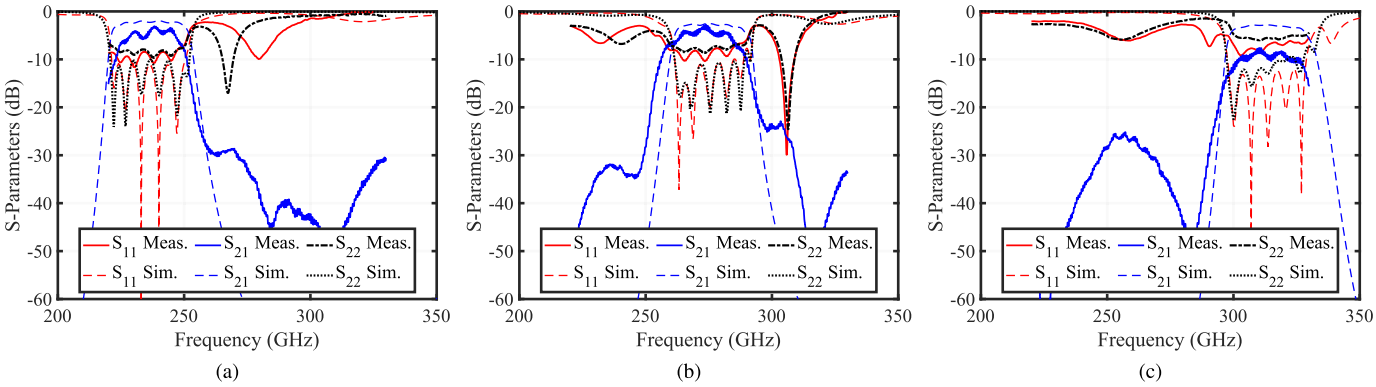

Fig. 15. Comparison of three individual channel filters, with wideband GSG transitions at both ends of the filters. (a) Channel 1 (220–250 GHz). (b) Channel 2 (260–290 GHz). (c) Channel 3 (300–330 GHz). The measured data is depicted as the solid line, with the corresponding full-wave simulation results shown as dotted lines. The forward transmission (S_{21}) and both ports' reflection (S_{11} and S_{22}) are plotted.

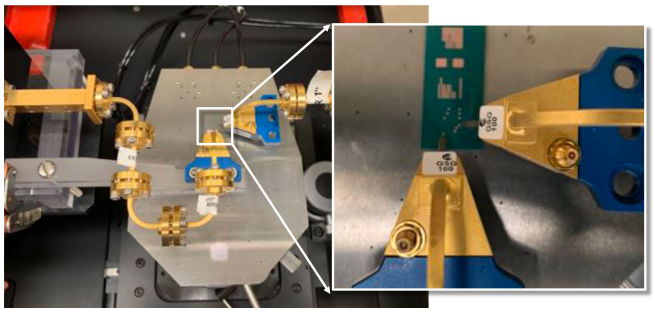

Fig. 16. Wafer-probe characterization of the triplexer.

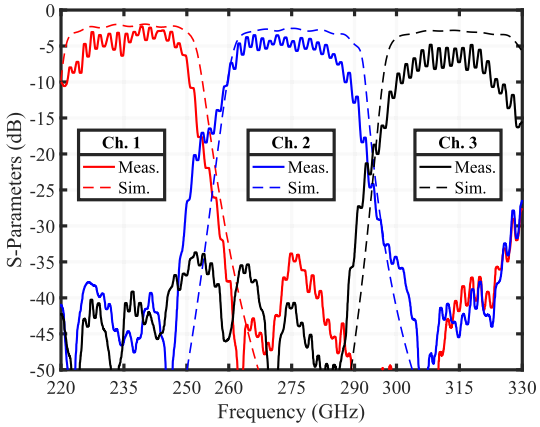

Fig. 17. Measured triplexer (two-port) response (solid lines) and the simulated two-port triplexer response based on a full-wave four-port model (dashed lines). The plotted data depicts the forward transmission of the two-port measurements, from the manifold to individual channel filter output ports.

of WR-3.4 and *H*-plane bends are used to position the waveguide probes appropriately for testing the triplexer.

When measuring the triplexer design, a multitier calibration scheme (including an unknown-through calibration [32]) is used to deembed the measurement setup from the device measurement.

1) A small section of WR-3.4 bend is characterized ($\mathbf{S_{bend}}$) independently after performing a two-port flange-flange calibration on a separate setup. The phase response of this section will be used in the subsequent unknown-through calibration.
2) Each VNA extender calibrated to the waveguide flange using a vendor-supplied waveguide calibration kit.
3) Each probe ($\mathbf{S_{left}}$ and $\mathbf{S_{right}}$) is characterized using the previous flange calibration to a set of vendor-supplied short, open, and load (SOL) standards on a calibration substrate.
4) The waveguide sections are attached to the VNA extenders up to the probes; the probes are not connected. A two-port unknown through calibration is utilized to move the calibration plane up to the probe flanges.
5) Finally, the probes are mounted, and the measured $\mathbf{S_{left}}$ and $\mathbf{S_{right}}$ responses for the left and right probes are used in the VNA to perform the final layer of deembedding to the probe tips.

At this point, the measurement setup is calibrated to a reference plane at the probe tips. The two-port device measurements can be taken. To account for larger calibration errors that were observed for wideband calibrations (compared with a test standard), this process was carried out for three sets of measurements. Each calibration and measurement covered 50 GHz of bandwidth: 220–270, 250–300, and 280–330 GHz. Each waveguide calibration was followed by the measurement of an offset short standard to ensure good calibration across the observation bandwidth. The plotted response includes averaging of those overlapping portions of the bands from each measurement (i.e., 250–270 and 280–300 GHz).

The simulated full-wave response in Fig. 11 is based on 50-Ω ports connected to all four triplexer ports. This full-wave four-port was simulated in three separate situations in Keysight ADS with the manifold (input) port connected and one of each of the channel filter ports connected. These simulated channel responses are plotted against the measured response in Figs. 17 and 18.

The frequency band is limited to no lower than 220 GHz due to the VDIs VNA extender and the available waveguide probes (WR-3.4) in the test setup. Fig. 17 shows the measured and simulated transmission of a two-port response of the triplexer structure; this represents a measurement (or simulation, shown with the dashed line) between the manifold and the associated channel filter output port. The other ports are unterminated.

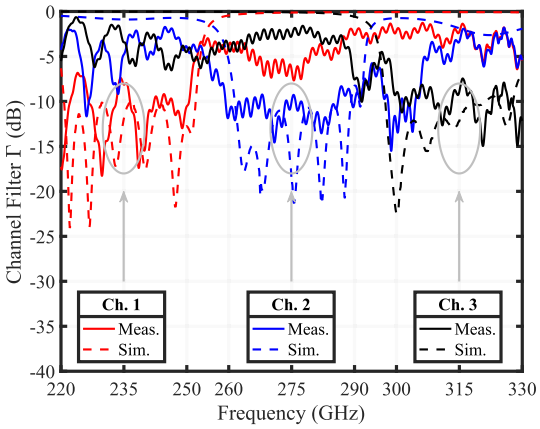

Fig. 18. Measured channel filter reflection of the triplexer (solid lines) and the simulated reflection based on a full-wave four-port model (dashed lines). These data correspond to the S_{22} measurement of a set of simulated and measured two-port tests.

TABLE II
PERFORMANCE COMPARISON WITH PUBLISHED WORK

Work	Oper. Band (GHz)	MUX FBW	Ch. FBW	IL (dB)	Size (λ_0^2)	Res. Type
This Work	220–330	40%	∼10%	∼3-7*	0.7-1.1*	Ridged SIW
[33]	525–625	17%	∼3%	∼0.5	199	Photonic Crystal
[34]	675–700	18.5%#	3.6%	∼2.1	-	RWG
[35]	305–357	-	15.4%	1.5	2.0	SIW
[36]	330–349	-	5.3%	0.6	1.9/542$	RWG

* - Per channel filter, incl. GSG transition. # - Estimated. $ - Packaged size.

The measured data were smoothed with an 800-MHz-wide Gaussian window. As can be seen in Fig. 15, the passband and stopband behaviors of the device correspond very well to the simulated response. The higher frequency ripple seen on the measured data is associated with phase mismatch between the VNA and the VDI frequency extenders. During calibration, phase mismatch is compensated for, but during measurement, any gross movement associated with the repositioning of the on-platen micropositioners and so on manifests itself as this type of high-frequency ripple.

Fig. 18 shows the measured and simulated channel filter reflection of the same scenarios. In this case, a 2-GHz-wide Gaussian window was used to smooth the data in order to resolve the structure in the channel filter reflections in channels 2 and 3. Again, the in-band response corresponds to the channel filter. The match in bands 2 and 3 from 220–250-GHz demonstrates an imperfect out-of-band reflection for those channels that will likely degrade the channel-to-channel isolation.

The mid-band insertion loss is approximately 2–4 dB larger than the simulated data. This may be attributed to losses associated with calibration and wafer probing and unmodeled copper roughness. There is some undesired spurious stopband transmission, which also may be attributed to imperfect calibration—especially at the lower signal to noise ratios physically present at the VNA extenders in the stopbands. Finally, one can see that the channel bandwidths are narrower than the device design. This is likely a function of small perturbations in resonator frequency and interresonator coupling. These could arise from small changes in fabricated dimensions or differences between modeled and fabricated material dielectric properties. Probe-landing locations can also be a source of inconsistency in the measurements. However, large changes in the measured responses were not observed with different positioning of the probes relative to the wideband transition pad openings. This may be attributed to the highly confined nature of these ridged-SIW structures and well-designed port matching.

V. CONCLUSION

The measured channel filters and triplexer responses demonstrate the efficacy of the presented device and design methodology. To the bets of our knowledge, this represents the first published instance of a ridged-SIW multiplexer implemented at these frequencies and operating over the demonstrated bandwidth. Furthermore, this work represents the first measured devices on an organic packaging process featuring continuous trench vias. Finally, this work also represents the best performance at these frequencies for these types of devices implemented in organic packaging technologies.

While the authors are unaware of any comparable published multiplexer implementation for this sub-THz application, the closest comparison in Table II is that shown in [33] though that work does not include any measurement results. It is a three-band channelizer over 525–625 GHz. However, the multiplexer bandwidth is 17% (compared with the 40% in the presented work) due to the narrow channel filter bandwidth. As was discussed in Section I, the device operating band is of the utmost importance. As such, fractional bandwidth of the multiplexer is an important figure of merit. The remaining comparisons [34]–[36] are sub-THz band single-channel filters and are listed to compare the fractional bandwidth of the single filter with our channel filter design. We note [35], in particular. This work compares favorably from a channel-filter perspective. However, as described in Section III-A, the spurious passband performance precludes the realization of wide operating band triplexers.

The device performance can, in the future, be improved by carefully characterizing the process material properties in the designed band along with the achievable fabrication tolerances and variations. These factors can be used to future improve the design of the channel filter and overall triplexer response by ensuring the location of the passband zeros. We expect that this will not only improve passband insertion loss and channel-to-channel isolation but also improvement manifold and channel filter matching.

The presented devices along with Intel's organic packaging process provide an attractive option for new, low-cost, high-performance, in-package filters, and multiplexers that can be readily integrated with existing IC infrastructure. The availability of these components can enable the realization of new millimeter-wave and THz systems.

ACKNOWLEDGMENT

The authors would like to thank Dr. Chris Galbraith at MIT Lincoln Laboratory, Dr. Luciano Boglione, and Dr. John

Rodgers at the Naval Research Laboratory for many helpful technical discussions. They would also like to thank Dr. Aleksandar Aleksov and the Substrate Process Technology Development Team, Intel Corporation, for the fabrication support.

REFERENCES

[1] J. W. Holloway, G. C. Dogiamis, and R. Han, "Innovations in terahertz interconnects: High-speed data transport over fully electrical terahertz waveguide links," *IEEE Microw. Mag.*, vol. 21, no. 1, pp. 35–50, Jan. 2020.

[2] M. Bozzi, A. Georgiadis, and K. Wu, "Review of substrate-integrated waveguide circuits and antennas," *IET Microw., Antennas Propag.*, vol. 5, no. 8, p. 909, 2011.

[3] X.-P. Chen and K. Wu, "Substrate integrated waveguide filter: Basic design rules and fundamental structure features," *IEEE Microw. Mag.*, vol. 15, no. 5, pp. 108–116, Jul. 2014.

[4] X.-P. Chen and K. Wu, "Substrate integrated waveguide filters: Design techniques and structure innovations," *IEEE Microw. Mag.*, vol. 15, no. 6, pp. 121–133, Sep. 2014.

[5] X.-P. Chen and K. Wu, "Substrate integrated waveguide filters: Practical aspects and design considerations," *IEEE Microw. Mag.*, vol. 15, no. 7, pp. 75–83, Nov. 2014.

[6] J. W. Holloway, L. Boglione, T. M. Hancock, and R. Han, "A fully integrated broadband sub-mmWave chip-to-chip interconnect," *IEEE Trans. Microw. Theory Techn.*, vol. 65, no. 7, pp. 2373–2386, Jul. 2017.

[7] S. Hu *et al.*, "A SiGe BiCMOS transmitter/receiver chipset with on-chip SIW antennas for terahertz applications," *IEEE J. Solid-State Circuits*, vol. 47, no. 11, pp. 2654–2664, Nov. 2012.

[8] Y. Shang, H. Yu, H. Fu, and W. M. Lim, "A 239–281 GHz CMOS receiver with on-chip circular-polarized substrate integrated waveguide antenna for sub-terahertz imaging," *IEEE Trans. THz Sci. Technol.*, vol. 4, no. 6, pp. 686–695, Nov. 2014.

[9] Z. Wang, P. Nazari, and P. Heydari, "Bottom-feed on-chip waveguide slot antenna for THz applications," in *Proc. IEEE Int. Symp. Antennas Propag. USNC/URSI Nat. Radio Sci. Meeting*, Jul. 2015, pp. 1458–1459.

[10] K. Dhwaj, Y. Zhao, R. A. Hadi, X. Li, F. M.-C. Chang, and T. Itoh, "A 0.55 THz on-chip substrate integrated waveguide antenna," in *Proc. 43rd Int. Conf. Infr., Millim., Terahertz Waves (IRMMW-THz)*, Sep. 2018, pp. 6–7.

[11] Y. Xiao, P. Shan, Y. Zhao, H. Sun, and F. Yang, "Design of a *W*-band GaAs-based SIW chip filter using higher order mode resonances," *IEEE Microw. Wireless Compon. Lett.*, vol. 29, no. 2, pp. 104–106, Feb. 2019.

[12] H. J. Tang, G. Q. Yang, J. X. Chen, W. Hong, and K. Wu, "Millimeter-wave and terahertz transmission loss of CMOS process-based substrate integrated waveguide," in *IEEE MTT-S Int. Microw. Symp. Dig.*, Jun. 2012, pp. 1–3.

[13] M. A.-D. Pino, H. T. Shivamurthy, D. Cavallo, L. Galatro, and M. Spirito, "BiCMOS integrated waveguide with artificial dielectric at submillimeter wave frequencies," in *IEEE MTT-S Int. Microw. Symp. Dig.*, May 2016, pp. 2–5.

[14] L. Wang, C. Zhang, M. Luo, C. Ma, and C. Jin, "W-band substrate integrated waveguide filter with," in *Proc. Asia–Pacific Microw. Conf. (APMC)*, no. 2, 2015, pp. 3–5.

[15] S. W. Wong, K. Wang, Z.-N. Chen, and Q.-X. Chu, "Design of millimeter-wave bandpass filter using electric coupling of substrate integrated waveguide (SIW)," *IEEE Microw. Wireless Compon. Lett.*, vol. 24, no. 1, pp. 26–28, Jan. 2014.

[16] M. Miao, X. Zhang, Y. Zhang, S. Xu, L. Liang, and Z. Li, "Design and simulation of THz filters embedded in LTCC multi-layer substrate," in *Proc. IEEE Int. Conf. Electron Devices Solid-State Circuits*, Nov. 2011, pp. 1–2.

[17] D. Stephens, P. R. Young, and I. D. Robertson, "Millimeter-wave substrate integrated waveguides and filters in photoimageable thick-film technology," *IEEE Trans. Microw. Theory Techn.*, vol. 53, no. 12, pp. 3832–3838, Dec. 2005.

[18] Z.-C. Hao, X.-P. Huo, W.-Q. Ding, and W. Hong, "Efficient design of compact contiguous-channel SIW multiplexers using the space-mapping method," *IEEE Trans. Microw. Theory Techn.*, vol. 63, no. 11, pp. 3651–3662, Nov. 2015.

[19] A. Corona-Chavez and T. Itoh, "Novel miniaturized triplexer using substrate integrated technology," in *Proc. Asia–Pacific Microw. Conf.*, 2010, pp. 678–681.

[20] R. Cameron and M. Yu, "Design of manifold-coupled multiplexers," *IEEE Microw. Mag.*, vol. 8, no. 5, pp. 46–59, Oct. 2007.

[21] G. Macchiarella, "Extraction of unloaded q and coupling matrix from measurements on filters with large losses," *IEEE Microw. Wireless Compon. Lett.*, vol. 20, no. 6, pp. 307–309, Jun. 2010.

[22] C. J. Galbraith and G. M. Rebeiz, "Higher order cochlea-like channelizing filters," *IEEE Trans. Microw. Theory Techn.*, vol. 56, no. 7, pp. 1675–1683, Jul. 2008.

[23] S. Hopfer, "The design of ridged waveguides," *IEEE Trans. Microw. Theory Techn.*, vol. MTT-3, no. 5, pp. 20–29, Oct. 1955. [Online]. Available: http://ieeexplore.ieee.org/document/1124972/

[24] C. Rauscher, S. W. Kirchoefer, J. M. Pond, A. C. Guyette, and D. R. Jachowski, "A compact ridge-waveguide contiguous-channel frequency multiplexer," *IEEE Trans. Microw. Theory Techn.*, vol. 57, no. 3, pp. 647–656, Mar. 2009.

[25] L. Li, X. Liang, Y. Zhang, X. Wang, S. Dong, and J. Xie, "Propagation characteristic of ridge substrate integrated waveguide," in *Proc. Int. Conf. Integr. Circuits Microsyst. (ICICM)*, Nov. 2016, pp. 195–199. [Online]. Available: http://ieeexplore.ieee.org/document/7813591/

[26] M. Bozzi, S. A. Winkler, and K. Wu, "Novel compact and broadband interconnects based on ridge substrate integrated waveguide," in *IEEE MTT-S Int. Microw. Symp. Dig.*, Jun. 2009, pp. 121–124. [Online]. Available: http://ieeexplore.ieee.org/document/5165647/

[27] C. A. Balanis, *Advanced Engineering Electromagnetics*. Hoboken, NJ, USA: Wiley, 1989.

[28] *ANSYS Electromagnetic Suite, Release 18.0*, ANSYS, Canonsburg, PA, USA, 2017.

[29] J. P. S. Sandhu, A. Girdhar, R. Ramakrishnan, R. D. Teja, and S. Ghosh, "FEST-3D: Finite-volume explicit STructured 3-dimensional solver," *J. Open Source Softw.*, vol. 5, p. 1555, Feb. 2020, doi: 10.21105/joss.01555.

[30] D. E. Zelenchuk, V. Fusco, G. Goussetis, A. Mendez, and D. Linton, "Millimeter-wave printed circuit board characterization using substrate integrated waveguide resonators," *IEEE Trans. Microw. Theory Techn.*, vol. 60, no. 10, pp. 3300–3308, Oct. 2012.

[31] M. Tlaxcalteco-Matus and R. Torres-Torres, "Modeling a SIW filter with IRIS windows using equivalent circuits," *Microw. Opt. Technol. Lett.*, vol. 54, no. 12, pp. 2865–2868, 2006. [Online]. Available: http://arxiv.org/abs/physics/0604155

[32] A. Ferrero and U. Pisani, "Two-port network analyzer calibration using an unknown 'Thru,'" *IEEE Microw. Guided Wave Lett.*, vol. 2, no. 12, pp. 505–507, Dec. 1992.

[33] J.-S. Li, H. Liu, and L. Zhang, "Compact and tunable-multichannel terahertz wave filter," *IEEE Trans. THz Sci. Technol.*, vol. 5, no. 4, pp. 551–555, Jul. 2015.

[34] D. Koller, E. W. Bryerton, and J. L. Hesler, "WM380 (675–700 GHz) bandpass filters in milled, split-block construction," *IEEE Trans. THz Sci. Technol.*, vol. 8, no. 6, pp. 630–637, Nov. 2018, doi: 10.1109/TTHZ.2018.2873114.

[35] F. Wang, V. F. Pavlidis, and N. Yu, "Miniaturized SIW bandpass filter based on TSV technology for THz applications," *IEEE Trans. THz Sci. Technol.*, early access, Feb. 14, 2020, doi: 10.1109/TTHZ.2020.2974091.

[36] N. Zhang, R. Song, M. Hu, G. Shan, C. Wang, and J. Yang, "A low-loss design of bandpass filter at the terahertz band," *IEEE Microw. Wireless Compon. Lett.*, vol. 28, no. 7, pp. 573–575, Jul. 2018.

Jack W. Holloway (Member, IEEE) received the B.S. degree in applied mathematics and electrical engineering and the M.Eng. degree in electrical engineering and computer science from the Massachusetts Institute of Technology (MIT), Cambridge, MA, USA, in 2003 and 2004, respectively, where he is pursuing the Ph.D. degree at the Department of Electrical Engineering and Computer Science (EECS).

He was an Officer in the United States Marine Corps from 2006 to 2019, serving as an F/A-18 Pilot, a Program Manager with Office of Naval Research (ONR), and a Technical Advisor with the Defense Innovation Unit (DIU), Office of the Secretary of Defense (OSD). He was a Visiting Researcher with the Naval Research Laboratory (NRL), Washington, DC, USA, from 2015 to 2020, and an MIT Lincoln Laboratory Military Fellow from 2015 to 2018. He is currently the Director of the Advanced Technology Division, Raytheon Missiles and Defense (RMD), Tewksbury, MA, USA.

Georgios C. Dogiamis (Member, IEEE) received the Dipl.Ing. degree in electrical and computer engineering from the National Technical University of Athens, Athens, Greece, in 2006, the M.Sc. degree in electrical engineering from the California Institute of Technology, Pasadena, CA, USA, in 2009, and the Ph.D. degree in electrical engineering from the University of Duisburg Essen, Duisburg, Germany, in 2014.

He was with the Informatics Department, Hellenic Army General Staff, Athens, from 2007 to 2009. Since 2009, he has been a Staff Researcher with the University of Duisburg-Essen and the Fraunhofer Institute (IMS), Duisburg. He joined the Components Research Team, Intel Corporation, Chandler, AZ, USA, in 2014, where he is currently a Senior Research Engineer. He holds more than 20 U.S. patents. His current research interests include flexible ultrathin circuits and sensors, millimeter-wave systems, and their associated packaging techniques.

Dr. Dogiamis is also a member of the Association of German Engineers.

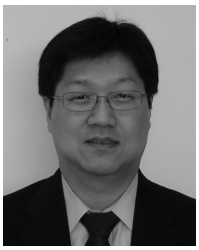

Sanghoon Shin (Senior Member, IEEE) received the B.S. degree from Hanyang University, Seoul, South Korea, in 1993, the M.S. degree in electrical engineering from the Polytechnic Institute of New York University, New York, NY, USA, in 1996, and the Ph.D. degree in electrical engineering from the New Jersey Institute of Technology (NJIT), Newark, NJ, USA, in 2002.

He joined RS Microwave Inc., Butler, NJ, USA, as a Research Engineer, in 2002. In 2010, he joined the U.S. Naval Research Laboratory (NRL), Washington, DC, USA, as a Staff Scientist. His research interests include broadband high-power filters and multiplexers and frequency-agile RF/Microwave filter design and analysis.

Dr. Shin has been serving as an Active Member of the IEEE MTT-T Technical Program Committee Member for Filters and Passive Components Committee (MTT-8) and the IEEE MTT-S Transaction Review Member of the Editorial Board since 2005. He has served as the Executive Officer of the IEEE North Jersey Section from 2003 to 2010.

Ruonan Han (Senior Member, IEEE) received the B.Sc. degree in microelectronics from Fudan University, Shanghai, China, in 2007, the M.Sc. degree in electrical engineering from the University of Florida, Gainesville, FL, USA, in 2009, and the Ph.D. degree in electrical and computer engineering from Cornell University, Ithaca, NY, USA, in 2014.

He has been with the Department of Electrical Engineering and Computer Science, Massachusetts Institute of Technology (MIT), Cambridge, MA, USA, since July 2014, where he is currently an Associate Professor. His research group at MIT focuses on RF-to-photonics integrated circuits and systems for spectroscopy, metrology, imaging, quantum sensing/processing, broadband/secure communication, and so on.

Dr. Han was a recipient of the Cornell ECE Directors Ph.D. Thesis Research Award, the Cornell ECE Innovation Award, and the Best Student Paper Awards of the IEEE Radio frequency Integrated Circuits Symposium in 2012 and 2017. He was also a recipient of the IEEE Microwave Theory and Techniques Society (MTT-S) Graduate Fellowship Award and the IEEE Solid-State Circuits Society (SSC-S) Predoctoral Achievement Award. He received the Intel Outstanding Researcher Award in 2019 and the National Science Foundation (NSF) CAREER Award in 2017. He was a Guest Associate Editor of the IEEE TRANSACTIONS ON MICROWAVE THEORY AND TECHNIQUES in 2019. He is also an Associate Editor of the IEEE TRANSACTIONS ON VERY LARGE SCALE INTEGRATION (VLSI) SYSTEM and the IEEE TRANSACTIONS ON QUANTUM ENGINEERING, and also serves on the Technical Program Committee (TPC) of the IEEE RFIC Symposium and the Steering Committee and a TPC of the IEEE International Microwave Symposium. He is also the IEEE MTT-S Distinguished Microwave Lecturer for the term 2020–2022.